

Degree of locality of elasto-optic response in solidsXin Liang¹ and Sohrab Ismail-Beigi^{1,2,*}¹*Department of Applied Physics, Yale University, New Haven, Connecticut 06520, USA*²*Department of Physics, and Department of Mechanical Engineering & Materials Science, Yale University, New Haven, Connecticut 06520, USA* (Received 18 March 2019; revised manuscript received 18 September 2019; published 10 December 2019)

The elasto-optic effect, or photoelasticity, describes the linear change of dielectric tensor with applied strain and is a universal material property of insulators and semiconductors. Though the elasto-optic responses for solids can be computed directly from first principles (e.g., by using density functional perturbation theory) and measured experimentally, these methods do not provide sufficient insight into the governing microscopic physical principles of photoelasticity. In this work, we describe a microscopic first-principles analysis of photoelasticity in real space and apply it to investigate the elasto-optic responses of Si, diamond, NaCl, and MgO. By writing the random phase approximation (RPA) dielectric constant in the basis of maximally localized Wannier functions, we show that the strain-dependent change of dipole transitions between occupied and unoccupied Wannier functions are the main determinants of photoelasticity. By organizing the dipole transitions into spatially localized shells, we develop a “constrained sum” method that converges both the dielectric and photoelastic responses systematically and reveals a relatively long-ranged nature to these responses: one needs to sum up contributions of up to third neighbor shells to converge the elasto-optic coefficient with reasonable precision.

DOI: [10.1103/PhysRevB.100.245204](https://doi.org/10.1103/PhysRevB.100.245204)**I. INTRODUCTION**

The elasto-optic effect, or photoelasticity, of a crystal describes the linear response change of optical refractive index with applied strain. By definition, only the electronic contribution to the dielectric response is included in the elasto-optic effect, and therefore it describes the strain dependence of the dielectric tensor at frequencies well above those of lattice vibrations but below the electronic band gap. The elasto-optic effect is of interest for technological applications as well as for fundamental science. For example, the elasto-optic effect reduces the efficiency of fiber Bragg gratings [1]. Next, semiconductor heterostructures in devices such as transistors have built-in interlayer strains due to the lattice mismatch between their constituent layers which, via the elasto-optic effect, modifies their electronic and optical properties. The elasto-optic effect also gives rise to birefringence phenomena in crystals by lowering their symmetries. For example, the normally isotropic dielectric constant in cubic solids turns into a rank-two tensor under strain, so that light will propagate with different speeds along different crystallographic axes. This effect has been used to make photoelastic modulators to modulate the polarization of light [2]. In nanoscale systems such as waveguides, the optical forces exerted by electromagnetic waves can be engineered by the elasto-optic effect through its relation with electrostrictive forces, enabling selective excitation of acoustic phonon modes in the waveguides [3]. The coupling between electromagnetic waves and acoustic phonons finds applications in making photonic-phononic

devices [4–8]. Since the magnitude and directions of the electrostrictive forces are determined by the elasto-optic and dielectric properties which have strong material dependences, they can be used to enhance or suppress the photon-phonon coupling. Hence, understanding and predicting elasto-optic response helps with the selection or design rules for materials for photon-phonon interactions.

Numerous computational works [9–13] have calculated the elasto-optic tensor for insulators and semiconductors using density functional theory (DFT) [14,15] and density functional perturbation theory (DFPT) [16]. DFPT is a powerful *ab initio* approach that can provide physical insight into the separate responses of electrons and ions, and the DFPT-computed elasto-optic tensors are in a good agreement with available experimental data. However, as a numerical method for response calculations, DFPT does not provide direct insight into the underlying physical principles of elasto-optic behavior in a localized, real-space manner in the sense detailed in Sec. II. There also exist phenomenological models for photoelasticity. Donadio and Bernasconi [13] developed a model to describe the photoelasticity of silica materials. Their model assumes that the dielectric response of silica is entirely determined by the sum over each oxygen atom’s polarizability which is affected by the local geometry of the crystal in response to strain. However, the attempt to generalize the model from silica to sodium silicate has been less successful [17]. Another model proposed by Damas *et al.* [18] centralized the role of individual chemical bonds in silicon and their response to lattice distortion based on bond orbital theory for tetrahedrally covalent crystals [19]. By analyzing how the bond polarizability changes with strain in Si, Damas *et al.* were able to extract the strain dependence of silicon’s dielectric tensor, i.e., the

*sohrab.ismail-beigi@yale.edu

elasto-optic effect. However, these phenomenological models include a variety of empirical parameters and assumptions on locality and short-ranged electronic response which must be verified and extracted from experimental data or *ab initio* calculations.

In this paper, we aim to understand the governing physical principles of the elasto-optic effect at the microscopic level from first principles. We first show that comparing to state-of-the-art DFPT calculations, the random phase approximation (RPA) presents a simple yet as accurate enough approach for describing the dielectric and elasto-optic responses. By rewriting the RPA formula for the dielectric tensor in the basis of maximally localized Wannier functions (MLWFs) [20], we discover that the strain-dependent dipole transitions between occupied and unoccupied Wannier functions are the main determinants of the elasto-optic effect. We also reveal a surprisingly long-ranged nature for the dielectric and elasto-optic response using the Wannier basis which means the basic assumptions of many semi-empirical approaches to photoelasticity should be reconsidered carefully. Four insulating materials from two distinct material classes are considered in this work: the covalent semiconductors Si and diamond, and the ionic crystals NaCl and MgO.

The structure of this paper is as follows. Section II describes the basic philosophy of this paper. Section III describes our computational methods. Section IV presents the state-of-the-art DFPT calculations for elasto-optic responses done in this work that are in good agreement with prior first-principles calculations and experiments. Section V is devoted to understanding the elasto-optic effect in silicon. Section VA compares the RPA and DFPT methods for calculating the photoelasticity of silicon and suggests that a promising venue to describe the elasto-optic effect is to use Wannier functions. It is also discovered in Sec. VA that the change of dielectric constant with strain is dominated by the dipole matrix elements rather than the eigenenergies of the Bloch states. Section VB furthers the discussion about the dipole transitions by rewriting the matrix elements into the Wannier basis. We then develop a “constrained sum” method in real space by partitioning dipole transitions into shells according to their distances. This “constrained sum” method reveals the long-ranged behavior of the dielectric and elasto-optic response of silicon which can be only understood intuitively in a localized basis set like Wannier functions. Sections VI–VIII apply the tools developed for Si to diamond, NaCl, and MgO. Similar conclusions about the locality of the photoelasticity can also be drawn for these three materials. We summarize the main findings, their implications and the relation of our work to the prior literature in Sec. IX.

II. PHYSICAL INSIGHT AND BOND-ORBITAL MODELS

As we will see in Sec. IV, fully *ab initio* approaches such as DFPT provide reliable tools for numerical computation of dielectric and photoelastic responses. However, such approaches do not provide sufficient insight in terms of a compact localized picture of the response that allows intuitive understanding and development of simple rules of thumb. More precisely, an ideal model would describe the materials response in terms of highly localized orbitals centered on the

atoms or bonds constituting the material. Prior work in this area has been based on Harrison’s bond orbital model [21]; in the simplest approximation, the linear dielectric susceptibility of a tetrahedral covalent solid (e.g., bulk silicon) can be written as

$$\chi_1 = Ne^2\gamma^2d^2\alpha_c^2/(12V_2),$$

where N is the mean valence electron density, e is the elementary charge, d is the equilibrium bond length between neighboring atoms, α_c is a parameter that describes the covalency of the bonds in the solid (in nonpolar materials such as Si, $\alpha_c = 1$), twice V_2 is equal to the energy splitting between the bonding and antibonding orbitals on the same chemical bond, and γ is an adjustable scaling parameter that is used to compensate for the discrepancies between the model and experimental data. All the parameters in the above expression for χ_1 relate to the physical properties of one single chemical bond. Therefore such a model possesses extreme locality, is straightforward to interpret, and, if accurate, provides an excellent starting point for materials design. Finding the strain dependencies of these parameters describes the photoelastic response within the bond-orbital picture. A recent example of this approach for elasto-optic response can be found in Ref. [18]. Despite the simplicity and easy interpretation of such models, the fact that the adjustable parameters such as γ can only be found by fitting to known materials properties limits their predictive power. Ideally, one would prefer to approach the problem using first principles in order to have predictive power for new materials.

Our fundamental aim in this paper is to answer two basic questions. First, how short-ranged is the photoelastic response when described in a localized bond-orbital type model developed from first principles? In other words, is this physical property short-ranged enough so that a simple physical picture emerges? Second, can the key parameters in the localized model be computed from first principles? Below, we will succeed in developing an *ab initio* real-space approach based on localized Wannier functions to compute the photoelastic response and find that the responses are longer ranged than assumed in the standard bond-orbital picture.

III. COMPUTATIONAL METHODS

The elasto-optic tensor p_{ijkl} is defined by the expression

$$\Delta\epsilon_{ij}^{-1} = p_{ijkl}e_{kl}, \quad (1)$$

where ϵ_{ij} is the dielectric tensor of the crystal and e_{kl} is the strain tensor. Therefore, the elasto-optic tensor p_{ijkl} is a rank-4 tensor with i, j, k, l being one of the x, y, z axial directions. The notation $\Delta\epsilon^{-1}$ describes the linear response change of ϵ . Since both the inverse dielectric tensor ϵ^{-1} and the strain tensor e are symmetric, the elasto-optic tensor possesses a number of permutation symmetries: $(i \leftrightarrow j)$ and $(k \leftrightarrow l)$ [22]. In this work, we use Voigt’s notation to compactify: $1 = xx, 2 = yy, 3 = zz, 4 = yz, 5 = xz, 6 = xy$. All the crystal structures studied in this paper (Si, diamond, NaCl, and MgO) have cubic symmetry at equilibrium which makes their elasto-optic tensors have only three independent components, i.e., p_{11}, p_{12} , and p_{44} .

TABLE I. Elasto-optic coefficients for bulk crystals (Si, diamond, NaCl, and MgO) obtained using DFPT. For Si, the results are provided for both equilibrium and strained lattices. For diamond, NaCl, and MgO, the elasto-optic coefficients based on one-sided (unparenthesized) and two-sided (parenthesized) finite differences using 1% strain are tabulated.

	DFPT (this work)	Prior first-principles calculation	Experiment
Si (unstrained)			
ϵ	12.986	13.200 [10], 10.468 [9]	11.830 [37]
p_{11}	-0.101	-0.098 [10], -0.111 [9]	-0.094 [37]
p_{12}	0.010	0.007 [10], 0.020 [9]	0.017 [37]
p_{44}	-0.050	-0.046 [10], -0.056 [9]	-0.051 [37]
Si (2.0% uniaxial strain along x)			
ϵ	13.356	—	—
p_{11}	-0.113	—	—
p_{12}	-0.010	—	—
Diamond			
ϵ	5.801	5.668 [9]	5.819 [38]
p_{11}	-0.263 (-0.262)	-0.264 [9]	-0.248 [39]
p_{12}	0.061 (0.063)	0.076 [9]	0.044 [39]
NaCl			
ϵ	2.508	2.615 [9]	2.380 [40]
p_{11}	0.058 (0.055)	0.077 [9]	0.115 [41]
p_{12}	0.153 (0.153)	0.157 [9]	0.161 [41]
MgO			
ϵ	3.127	3.160 [13], 3.077 [9]	3.020 [42]
p_{11}	-0.299 (-0.301)	-0.310 [13], -0.218 [9]	-0.259 [42]
p_{12}	-0.042 (-0.041)	-0.050 [13], 0.013 [9]	-0.011 [42]

In this work, we use density functional theory (DFT) [14,15] to compute the electronic structure of bulk crystals using the QUANTUM ESPRESSO software package [23] with periodic boundary conditions and a plane-wave basis. We use the local density approximation (LDA) [24–26] for exchange and correlation and employ norm-conserving pseudopotentials [27,28] to describe the ionic cores. The four bulk crystals in this paper are all simulated using two-atom primitive unit cells with their experimental lattice constants of $a_0 = 5.43, 3.57, 5.64,$ and 4.21 \AA for Si, diamond, NaCl, and MgO, respectively [29]. A $6 \times 6 \times 6$ uniform k -point grid sampling with appropriate energy cutoff (35 Ry for Si, 60 Ry for diamond, 30 Ry for NaCl, and 65 Ry for MgO) achieves total energy convergence within 1 meV/atom. To calculate the static dielectric constant of solids, we use density functional perturbation theory (DFPT) [16] as implemented in QUANTUM ESPRESSO. Since we are interested in describing the change of the dielectric response with strain rather than the dielectric response itself, further analysis reveals that a $12 \times 12 \times 12$ uniform k grid sampling is needed to converge the change of dielectric constant to 0.01 in absolute value with 1% uniaxial strain.

We also use the random phase approximation (RPA) to compute dielectric response [30,31]. The RPA is very useful because it is written as an explicit analytical formula. Our results will show that the RPA provides a highly satisfactory approximation to the more accurate DFPT results for both the dielectric tensor and its strain dependence. We use the expression for the longitudinal RPA dielectric constant given by

$$\epsilon = 1 + \frac{16\pi}{V} \times \frac{1}{|q|^2} \sum_{\mathbf{k}} \sum_{c,v} \frac{|\langle \psi_{c,\mathbf{k}} | e^{-i\mathbf{q}\cdot\mathbf{r}} | \psi_{v,\mathbf{k}+\mathbf{q}} \rangle|^2}{E_{c,\mathbf{k}} - E_{v,\mathbf{k}+\mathbf{q}}}, \quad (2)$$

where $V = N_{\mathbf{k}} \Omega$ is the volume of the super cell which is equal to number of k points $N_{\mathbf{k}}$ multiplied by the volume of the primitive cell Ω . The summation ranges over all pairs of valence (v , occupied) and conduction bands (c , unoccupied) and also the whole Brillouin zone (\mathbf{k}). The wave vector \mathbf{q} is that of the external electric field applied to the material, but since photoelasticity is a long-wavelength response (i.e., uniform imposed electric field), we let $|\mathbf{q}|$ approach zero ($|\mathbf{q}|$ is set to be 1% of a primitive reciprocal lattice vector in our calculations).

We aim to use an accurate first-principles real-space representation for dielectric response in solids, especially for the $\langle e^{-i\mathbf{q}\cdot\mathbf{r}} \rangle$ dipole matrix elements in (2). A natural choice is to utilize maximally localized Wannier functions (MLWFs) [20,32,33] as the basis set. For a selected set of energy bands, MLWFs span the same Hilbert space as Bloch states since they are constructed by unitary transformation of the Bloch states. MLWFs are exponentially localized in real space [34], which is a desired feature when describing a system's locality. The mathematical expression for MLWFs is

$$W_{n,\mathbf{R}}(r) = \frac{1}{\sqrt{N_{\mathbf{k}}}} \sum_{\mathbf{k}} \sum_{m=1}^J e^{-i\mathbf{k}\cdot\mathbf{R}} \psi_{m,\mathbf{k}}(r) \times U_{m,n}^{(\mathbf{k})}. \quad (3)$$

where $U^{(\mathbf{k})}$ are rectangular $J \times N_{\text{wann}}$ unitary matrices representing the gauge freedom in building Wannier functions, J is the number of bands targeted to make Wannier functions whereas N_{wann} is the number of Wannier functions wanted per unit cell. The $U^{(\mathbf{k})}$ are determined to achieve the maximal locality criterion [32]. Wannier functions in this work are generated using the WANNI90 software package [35,36].

Wannier functions in this work are generated separately for valence and conduction bands so that we can describe dipole transitions between filled (valence) and empty (conduction)

Wannier functions in real space. The spatial characters of the generated Wannier functions are determined by the chemistry of the solids (detailed in Secs. V–VIII). For example, for each two-atom primitive unit cell of silicon, we generate four bonding Wannier functions for the four valence bands and then disentangle the low lying conduction bands to generate four antibonding Wannier functions. The eight Wannier functions basis per cell form a “minimum basis set” in a tight-binding model for silicon crystal. By substituting the relation between MLWFs and Bloch states from Eq. (3) into Eq. (2), we arrive at an expression for the RPA dielectric constant in the MLWF basis:

$$\epsilon = 1 + \frac{16\pi}{V} \times \frac{1}{|q|^2} \times \sum_{a,b,\mathbf{R}} \sum_{a',b',\mathbf{R}'} M_{a',b',\mathbf{R}'}^* \times M_{a,b,\mathbf{R}} \times F_{a',b',\mathbf{R}';a,b,\mathbf{R}}, \quad (4)$$

where

$$M_{a,b,\mathbf{R}} = \langle W_{a,\mathbf{R}} | e^{-i\mathbf{q}\cdot\mathbf{r}} | W_{b,0} \rangle, \quad (5)$$

$$F_{a',b',\mathbf{R}';a,b,\mathbf{R}} = \frac{1}{N_{\mathbf{k}}} \sum_{c,v,\mathbf{k}} e^{-i\mathbf{k}\cdot(\mathbf{R}-\mathbf{R}')} \times \frac{U_{ca'}^{(\mathbf{k})*} U_{ca}^{(\mathbf{k})} U_{vb'}^{(\mathbf{k})} U_{vb}^{(\mathbf{k})*}}{E_{c,\mathbf{k}} - E_{v,\mathbf{k}+\mathbf{q}}}. \quad (6)$$

The summation over \mathbf{R}, \mathbf{R}' in Eq. (4) ranges over all lattice vectors in the supercell. Equation (5) is the Wannier dipole matrix element connecting a bonding state in the “home” unit cell (at $\mathbf{R} = 0$) to an antibonding state in unit cell \mathbf{R} . Equation (6) is the Fourier transform of the energy difference denominator in the Bloch representation, and $U_{ca}^{(\mathbf{k})}$ and $U_{vb}^{(\mathbf{k})}$ are the unitary matrices mixing conduction and valence bands to make antibonding and bonding Wannier functions, respectively. Equation (4) is a sum over all pairs of dipole transitions in the supercell modulated by the Fourier transform of the energy denominator.

Making the unitary transformation of the basis from Bloch states in Eq. (2) to Wannier functions in Eq. (4) permits us to analyze the spatial behavior (e.g., locality) of the dielectric response. While it is hard to guess the behavior of ϵ versus increasing size of the k -point mesh in Eq. (2), the real-space version of Eq. (4) is more transparent to analyze since we are increasing the size of the supercell by including longer \mathbf{R} vectors. As \mathbf{R} grows, $M_{a,b,\mathbf{R}}$ will decrease since it involves the overlap of two Wannier functions that are at growing separations: we expect the sum in Eq. (4) to converge as successively larger \mathbf{R} vectors are included. In addition, we can make a reasonable guess (verified numerically below) on the type of convergence that will be seen. Since $F_{a',b',\mathbf{R}';a,b,\mathbf{R}}$ in Eq. (6) is the unitary transform of the energy difference denominator $\frac{1}{E_{c,\mathbf{k}} - E_{v,\mathbf{k}+\mathbf{q}}}$ (which is a positive definite quantity), $F_{a',b',\mathbf{R}';a,b,\mathbf{R}}$ is also a positive-definite matrix. We can compactify and rewrite Eq. (4) via the inner product of M with itself through F , $M^\dagger \times F \times M$, as

$$\epsilon = 1 + \frac{16\pi}{V} \times \frac{1}{|q|^2} \times M^\dagger \times F \times M, \quad (7)$$

where we have compactified the indexing of the vector M_l and the matrix F_{lm} using collective indices $l = (a, b, \mathbf{R})$. The Fourier-transform nature of F indicates that it is diagonally

dominant (i.e., largest when $\mathbf{R} = \mathbf{R}'$) so that as we add longer \mathbf{R} to the sum to achieve convergence, we can expect the convergence to be monotonically increasing since we are adding more contributions from of a positive-definite matrix. We will build on this idea below to understand the spatial locality of dielectric constant in the Wannier basis (detailed in Secs. V–VIII).

As will become evident below, the RPA approach to computing dielectric and photoelastic response is not as numerically accurate as DFPT; the RPA is missing a number of physical effects including local field corrections as well as the effects of exchange and correlation on screening. However, the primary utility of the RPA lies in its simplicity in the form of an analytical formula that can then be used to derive a localized form *ab initio* for the dielectric response; in addition, the numerical results below show that the RPA approach is quantitative (for Si, diamond, and MgO) or at least semiquantitative (for NaCl) when computing photoelastic response.

IV. DFPT

We begin by presenting computed results for the dielectric and elasto-optic tensors of bulk Si, diamond, NaCl, and MgO using DFPT which lay the groundwork for the results that we wish to understand using a more detailed analysis.

Cubic crystals, like the ones studied in this work, have only three independent components in their elasto-optic tensors, namely, p_{11} , p_{12} , and p_{44} . Elasto-optic coefficients computed from DFPT for these materials at the experimental lattice constant are reported in the first column of Table I. We use a $12 \times 12 \times 12$ k -point grid (unless otherwise specified) for the calculations in this work. We impose uniaxial strain along the x direction on the bulk to compute p_{11} and p_{12} and off-diagonal shear strain (with e_{23} being the only nonzero component in the strain tensor) to compute p_{44} . For uniaxial strain, we move the atoms proportionally with strain. For off-diagonal e_{23} strain, we strain the unit cell first and then relax the atoms inside the strained cell. For silicon, for each independent deformation, we compute the inverse dielectric tensor for several different strain values and then interpolate them using third order polynomials (in strain) to obtain the elasto-optic tensor. Results are also benchmarked against higher order polynomial interpolations (up to fifth order) and finite difference formulae to ensure numerical stability to within the quoted number of digits in Table I. For diamond, NaCl, and MgO, only the elasto-optic responses related to uniaxial strain are computed. In these three materials, we compute the inverse dielectric tensor at equilibrium and 1% uniaxial strain along the x axis and use the finite difference formula to extract the p_{11} and p_{12} components. We have checked explicitly that 1% strain is small enough to give precise enough results for further analysis below: the table shows that using simple one-sided versus the higher order two-sided finite differencing makes very little difference for the computed p_{11} and p_{12} values.

From Table I, we observe that our results for both the static dielectric constant and the elasto-optic tensor are in semiquantitative agreement with experiments and prior first-principles calculations except for MgO’s p_{12} component from Ref. [9]. The effect of finite wavelength λ of the electric field

TABLE II. Elasto-optic coefficients for bulk Si obtained using the RPA compared with DFPT.

	DFPT	RPA (100 bands)	RPA (12 bands)	RPA (8 bands)
Si (unstrained)				
ϵ^∞	12.986	13.823	13.805	13.629
p_{11}	-0.101	-0.094	-0.094	-0.099
p_{12}	+0.010	+0.008	+0.008	+0.010
Si (2.0% uniaxial strain along x)				
p_{11}	-0.113	-0.106	-0.106	-0.111
p_{12}	-0.010	-0.011	-0.011	-0.010

on photoelasticity in MgO has been investigated by Erba and Dovesi [9] and is reported to change the sign of p_{12} when λ goes from 400 to 1400 nm. The experimental values of p_{12} for MgO are scattered; e.g., the measurement of Giardini and Poindexter [43] has a different sign of p_{12} compared to the other measurements [42,44]. The discrepancies of the sign of p_{12} reported from experiments also suggest that the accurate determination of p_{12} in MgO is also a nontrivial task and requires future work. Overall, we find that DFPT is a reliable tool for predicting or computing the elasto-optic tensor of solids. We also report the elasto-optic tensor for silicon in a strained configuration in Table I. It is worth noting that one can tune the elasto-optic response of silicon crystal by deformation. Interestingly, the p_{12} elasto-optic coefficient even changes sign from +0.010 to -0.010 when silicon is strained uniaxially by 2%. In addition, Table I also shows the intriguing fact that NaCl and MgO, which have the same crystal structure and similar chemical properties, have the opposite elasto-optic response in both p_{11} and p_{12} components. These surprises, found in both computations and experiments, provide further motivation for studying the microscopic basis of photoelasticity.

V. SILICON

A. RPA

We use the RPA formula Eq. (2) to compute the dielectric response of bulk Si using the same procedure as for DFPT. We can see from the tabulated data that the RPA provides p_{11} and p_{12} coefficients that are very close to the DFPT values. In addition, the RPA offers a simple mathematical expression [Eq. (3)] that allows us to do further analysis below. Table II shows that both the static dielectric constant and the elasto-optic tensor converge quickly with total number of bands. Using only eight bands, i.e., four valence and four lowest conduction bands, the results are good enough to capture the main features of the elasto-optic response. In addition, eight bands also represent the minimal sp^3 basis needed for a tight-binding model for bulk Si which allows further analysis of the photoelasticity.

To study the convergence of the dielectric response versus k sampling, we separate out the contribution to ϵ from each k point:

$$\epsilon = 1 + \sum_{\mathbf{k}} D(\mathbf{k}), \quad (8)$$

where

$$D(\mathbf{k}) = \frac{16\pi}{V} \times \frac{1}{|q|^2} \sum_{c,v} \frac{|\langle \psi_{c,\mathbf{k}} | e^{-i\mathbf{q}\cdot\mathbf{r}} | \psi_{v,\mathbf{k}+\mathbf{q}} \rangle|^2}{E_{c,\mathbf{k}} - E_{v,\mathbf{k}+\mathbf{q}}} \quad (9)$$

in Eq. (2) is a delocalized quantity in momentum space: we can see from Fig. 1 that the cumulative sum of $D(\mathbf{k})$ slowly converges to $\epsilon - 1$, meaning that one cannot single out a small subset of k points that can account for most of the contribution to dielectric response. Figure 1 also shows that the change of dielectric constant $\Delta\epsilon$ due to strain is somewhat more localized in k space than ϵ , but we still need a significant fraction of the total number of k points to converge the cumulative sum of $\Delta D(\mathbf{k})$.

We find that the changes of dipole matrix elements ($e^{-i\mathbf{q}\cdot\mathbf{r}}$) with strain plays a more important role than the changes of Bloch eigenenergies $E_{n,\mathbf{k}}$ in determining a material's photoelasticity. We can separate the impacts of these two factors in this way: we compute the dielectric constant ϵ_{xx} at a strained

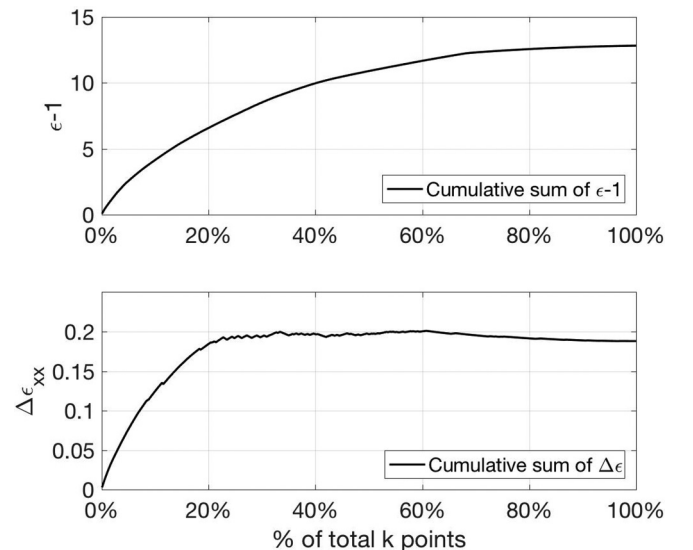


FIG. 1. Cumulative sum of $D(\mathbf{k})$ and $\Delta D(\mathbf{k})$ with 1.0% uniaxial strain along x axis in bulk Si. The horizontal axis is the fraction of k -points in the total $12 \times 12 \times 12 = 1728$ k -point mesh. In the upper plot of the cumulative sum of $D(\mathbf{k})$, the k points are sorted by magnitude of $D(\mathbf{k})$ in decreasing order; in the lower plot of the cumulative sum of $\Delta D(\mathbf{k})$, which is the change in $D(\mathbf{k})$ due to the imposed 1.0% strain along x axis, the k points are sorted by magnitude of $\Delta D(\mathbf{k})$ in decreasing order.

TABLE III. Dielectric constant for bulk Si using RPA. The first and second columns are the dielectric constant at equilibrium and its change with 1% uniaxial strain along the x -axis. In the third and fourth columns, $\Delta\epsilon_{xx}$ is computed by calculating the dielectric constant at the strained configuration with either the dipole matrix elements $\langle\psi_{c,k}|e^{-iq\cdot r}|\psi_{v,k+q}\rangle$ or eigenenergies $E_{n,k}$ in Eq. (2) fixed to their equilibrium values.

ϵ	$\Delta\epsilon_{xx}$	$\Delta\epsilon_{xx}$ (fixed $(e^{-iq\cdot r})$)	$\Delta\epsilon_{xx}$ (fixed $E_{n,k}$)
13.823	0.188	-0.027	0.083

configuration using Eq. (4) with either the dipole matrix elements $\langle\psi_{c,k}|e^{-iq\cdot r}|\psi_{v,k+q}\rangle$ or eigenenergies $E_{n,k}$ fixed at their equilibrium values. Table III shows that the change of dielectric constant in Si is dominated by the dipole matrix elements rather than the eigenenergies. In fact, evaluating the dielectric constant for strained silicon while keeping the $\langle e^{-iq\cdot r} \rangle$ at the equilibrium value will give a change of dielectric response $\Delta\epsilon_{xx}$ in the wrong direction. This also agrees with Detraux and Gonze’s assessment about the influence of the deformation potential (i.e., the change of electronic eigenenergies with lattice deformation) on the photoelasticity [45]. These observations warrant our continued investigations of elasto-optic response while focusing on the role of the dipole transition matrix elements.

While the delocalization of the dielectric response in k space is not helpful, it does point to a possible path forward. The adequacy of eight energy bands combined with the delocalized nature of dielectric response in k space strongly suggests that using a basis set localized in real space may be more fruitful for understanding the photoelasticity of Si.

B. Wannier analysis and unexpected convergence behavior

We begin by generating four bonding and four antibonding Wannier functions for each two-atom primitive cell in bulk Si. These Wannier functions come in pairs: each pair consists of a bonding and an antibonding Wannier function centered on the same chemical bond between two nearest-neighbor silicon atoms. (The bonding/antibonding pair on a bond are physically identical to those on other bonds by appropriate translations and rotations.) Figure 2 shows one bonding/antibonding pair. The description of the electronic structure given by these Wannier functions is consistent with the localized chemical picture where two sp^3 hybrid orbitals from neighboring silicon atoms overlap and form a chemical bond. The interpolated band structure (Fig. 3) using these Wannier functions shows that they reproduce the DFT bands accurately for both valence and conduction bands around the Fermi energy.

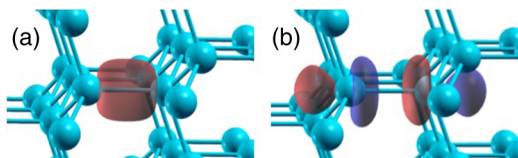


FIG. 2. Wannier functions in bulk Si: (a) bonding and (b) antibonding. Red and blue correspond to positive and negative values in these isosurface plots, respectively. These isosurface plots demonstrate that the bonding and antibonding maximally localized Wannier functions are localized in real space about the center of a Si-Si bond.

We compute the dielectric tensor of bulk Si in the Wannier function basis using Eq. (4) for bulk Si at equilibrium and with 1% uniaxial strain and 1% shear strain. Table IV shows that the Wannier function method with the four bonding and four antibonding orbitals agrees well with RPA results with eight bands for both the dielectric constant and its change under uniaxial strain. The small differences between the eight-band RPA method and the Wannier method are a consequence of the disentanglement procedure used in building the antibonding Wannier functions: the disentanglement procedure selects the subspace of Bloch states that are “smoothest” across k space [33], which is not equivalent to reproducing the four lowest energy-sorted conduction bands (see Fig. 3). Our method for computing the full dielectric tensor is detailed in the Appendix. The changes $\Delta\epsilon_{xx}$, $\Delta\epsilon_{yy}$, and $\Delta\epsilon_{yz}$ are shown in Table IV since they are related directly to the computation of the p_{11} , p_{12} , and p_{44} photoelastic components. The small nonzero value of the ϵ_{yz} component at zero strain (equilibrium) is due to the fact that standard Monkhorst-Pack k grid used for the two-atom primitive cell does not obey the full crystalline symmetry of Si (but the grid is dense enough to give only small numerical asymmetries).

Having established the sufficient accuracy of the Wannier method, we now analyze the spatial locality of the dielectric response of bulk Si using Wannier functions. We begin by investigating the decaying behavior of the Wannier dipole

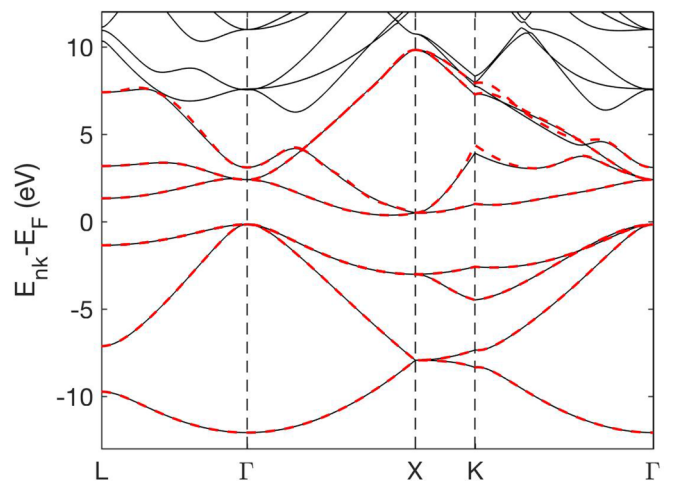


FIG. 3. Band structure of bulk Si. Black solid lines are the DFT-LDA bands; red dashed lines are the Wannier interpolated bands. Since the frozen window [33] ranges from below the valence band to a few eV above the Fermi energy, the valence and low-lying conduction bands are reproduced exactly; as shown in the text, the differences at higher energies only lead to small errors in the computed dielectric response in the Wannier basis.

TABLE IV. The dielectric constant and its change with 1% uniaxial strain along the x axis (first three rows of the table) and the ϵ_{yz} component of dielectric tensor and its change with $e_{23} = 1\%$ shear strain (last two rows of the table) for Si. The results in the table are based on a $12 \times 12 \times 12$ grid and are obtained using DFPT, using the RPA with Bloch states from Eq. (2), and using Wannier functions from Eq. (4) (see the Appendix for the equations used to compute the full dielectric tensor).

	DFPT	RPA (100 bands)	RPA (12 bands)	RPA (8 bands)	Wannier
ϵ (0.0%)	12.985	13.823	13.805	13.629	13.553
$\Delta\epsilon_{xx}$ (1.0%)	0.178	0.188	0.188	0.194	0.199
$\Delta\epsilon_{yy}$ (1.0%)	-0.008	-0.006	-0.006	-0.008	-0.004
ϵ_{yz} (0.0%)	0.000	0.005	0.005	0.005	0.005
$\Delta\epsilon_{yz}$ (1.0%)	0.081	0.093	0.093	0.093	0.094

matrix element M [Eq. (5)] as a function of distance (see Fig. 4) with \mathbf{q} aligned along the x axis. Figure 4 shows that the dipole matrix element has a rather “long tail”, i.e., the magnitude is still non-negligible even when the centers of bonding and antibonding Wannier functions are many bond lengths apart. This means the dielectric response in the Wannier basis has relatively long-ranged behavior, which is unexpected since maximally localized Wannier functions are expected to be quite compact. We infer that the dipole matrix element becomes longer-ranged than the Wannier functions themselves due to the long-ranged nature of the position operator: the lowest order contribution for small \mathbf{q} is $e^{-i\mathbf{q}\cdot\mathbf{r}} \approx 1 - i\mathbf{q}\cdot\mathbf{r}$, and due to the orthogonality of Wannier functions, $M \approx -\langle W_{a,\mathbf{R}} | i\mathbf{q}\cdot\mathbf{r} | W_{b,0} \rangle$ which highlights how the long-ranged position operator \mathbf{r} can give rise to long-ranged dipole matrix elements.

Such long-ranged behavior also manifests itself in the convergence of the dielectric constant with increasingly dense k -point meshes or equivalently larger real-space supercells. In k space, a periodic supercell is represented by a uniform

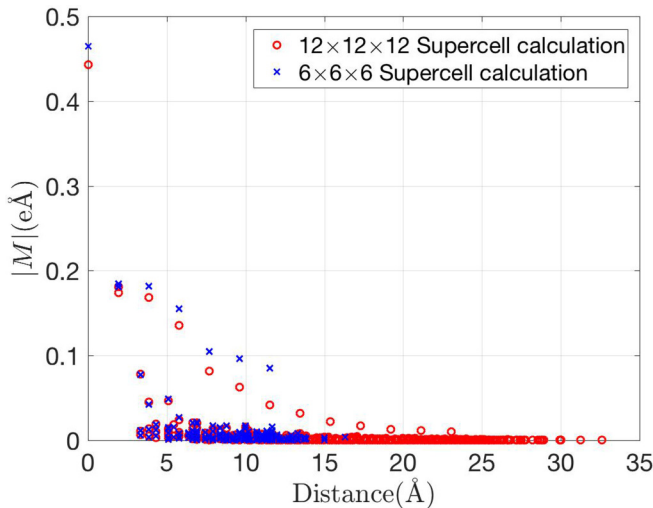


FIG. 4. Magnitude of the Wannier dipole matrix elements $|M|$ [Eq. (5)] vs distance between Wannier functions. Wave vector \mathbf{q} is aligned with x axis. The distance is between the center of $W_{b,0}$ (the bonding Wannier function in the home unit cell) and $W_{a,\mathbf{R}}$ (the antibonding Wannier function \mathbf{R} lattice vectors away). For reference, the bond length between nearest-neighbor Si atoms is 2.35 \AA . The two sets of results are for Wannier functions generated in two different supercells.

Born-von Karman k -point sampling of the Brillouin zone; in real space, the supercell is represented by a large volume of material on which periodic boundary conditions are imposed. The diagonal entries of Table V represent a “standard” convergence calculation: we increase the size of the supercell, generate Wannier functions, and compute the dielectric response using the full supercell’s worth of data. We can see that the ϵ_{xx} is not quite converged even for a $12 \times 12 \times 12$ supercell. In the k -space view, slow convergence with the density of the k -point sampling represents a “long-ranged” quantity. However, based on the equivalence of k -point mesh in the RPA method [Eq. (2)] and the size of supercell in the Wannier method [Eq. (4)], the monotonically decreasing dielectric constant (see blue dashed line in Fig. 5) with increasing k -point mesh is counterintuitive since, as discussed in Sec. III, we might expect that by including dipole transitions between Wannier functions further apart in a larger supercell, the dielectric constant should increase.

To shed further light on this unexpected convergence behavior, we employ Eq. (4) in a different manner as a “constrained sum.” We generate Wannier functions for a large supercell but constrain the sum over lattice vectors \mathbf{R}, \mathbf{R}' in Eq. (4) to range over a smaller subset centered on the origin that represents a smaller supercell. In this way, we can disentangle the change of the spatial form of the Wannier functions themselves with supercell size from the actual locality of the dipole matrix elements and energy denominators [$M_{a,b,\mathbf{R}}$ and $F_{a',b',\mathbf{R}';a,b,\mathbf{R}}$ in Eq. (4)]. Namely, we only include the dipole matrix elements $M_{a,b,\mathbf{R}}$ [Eq. (5)] whose bonding Wannier function $W_{b,0}$ and antibonding Wannier function $W_{a,\mathbf{R}}$ both fall inside the smaller $x \times x \times x$ supercell centered around origin. For example, in the last column of Table V, we vary x from 6 to 12, and the dielectric constant convergences in an increasing manner (see Fig. 5). Similar convergence is also observed in the $8 \times 8 \times 8$ and $10 \times 10 \times 10$ columns in Table V. Despite the more sensible convergence behavior, we confirm the long-ranged nature of the dielectric response within this “constrained sum” method. In fact, for Wannier functions generated in $12 \times 12 \times 12$ supercell, including the dipole transitions between Wannier functions on the same, nearest-neighbor, and second-nearest-neighbor chemical bonds together only accounts for 50% of the total dielectric response when using the subset $x = 2$ (see last column of Table V).

The above results provide the following physical picture. For a fixed sets of Wannier functions generated in a large supercell, one sees sensible convergence from below for the

TABLE V. Convergence of dielectric constant in bulk Si using the Wannier RPA method. The columns represent the size of supercell used to generate the Wannier functions. The rows represent the subset of the supercell whose dipole transition are summed up to obtain the dielectric constant. The numbers without parentheses are the dielectric constant ϵ_{xx} of bulk Si at equilibrium; the numbers in parentheses are the change of dielectric constant $\Delta\epsilon_{xx} = \epsilon_{xx}(1.0\%) - \epsilon_{xx}(0.0\%)$ of Si strained uniaxially by 1.0% along the x axis.

		Size of supercell used to generate Wannier functions			
		$6 \times 6 \times 6$	$8 \times 8 \times 8$	$10 \times 10 \times 10$	$12 \times 12 \times 12$
Subset of Wannier functions used	$2 \times 2 \times 2$	5.94(0.10)	5.53(0.08)	5.43(0.08)	5.41(0.08)
	$4 \times 4 \times 4$	11.89(0.19)	10.62(0.15)	10.34(0.16)	10.27(0.16)
	$6 \times 6 \times 6$	16.87(0.23)	13.11(0.17)	12.55(0.19)	12.43(0.18)
	$8 \times 8 \times 8$	—	14.59(0.18)	13.36(0.19)	13.16(0.19)
	$10 \times 10 \times 10$	—	—	13.81(0.20)	13.41(0.20)
	$12 \times 12 \times 12$	—	—	—	13.55(0.20)

dielectric response upon adding more distant contribution in real space: this is physically what we expect for a localized real-space representation. Hence, the unexpected behavior of dielectric response versus supercell size in the “standard” computations must be due to the Wannier functions themselves changing as they are generated in progressively larger supercells. In fact, the Wannier functions generated in smaller supercells must be longer ranged so that they lead to overestimation of the dipole elements and the dielectric response. This behavior also makes sense: Wannier functions generated in a periodic supercell are necessarily periodic as well because of the overall Born-von Karman periodic boundary condition; when the supercell is not large enough, the periodized Wannier functions will include the periodic images of the true (infinite supercell) Wannier functions in the tail regions summed from adjacent supercells. While the errors in the Wannier function tails are small, they are sizable enough to lead to the misleading convergence with supercell size. Figure 4 shows how the $6 \times 6 \times 6$ and $12 \times 12 \times 12$ supercells differ quantitatively for the same dipole matrix elements M due to the Wannier functions themselves changing with supercell size. We conclude that the artificial periodicity of the supercell Wannier functions is the root of the convergence behavior in the “standard” calculation.

We build on the constrained sum method to further analyze the spatial locality of the change of the dielectric constant

with strain. First, the Wannier dipole transition matrix elements can be spatially grouped into shells: each shell includes the dipole transitions that are related to each other through crystal symmetry. Hence, dipole transitions belonging to the same shell have the same distance between the bonding and antibonding Wannier functions, and we sort them by distance. We focus on the first three shells of the dipole transitions with largest matrix element from Fig. 4 and show them graphically in Fig. 6. Table VI displays the matrix elements from the three shells and how they change with applied strain. Table VI shows that increasing distance reduces the dipole transition strength, but the rate of decrease is modest: matrix elements between the same chemical bond, nearest-neighbor bonds, and second-nearest-neighbor bonds still have the same order of magnitude. The change of the matrix elements with strain is more complicated: Table VI shows that $|M|$ can either become larger or smaller depending on the type of imposed strain.

Now we analyze the locality of the change of the dielectric constant using the constrained sum method. Table VI shows that all three shells are required to reach a reasonable convergence of $\Delta\epsilon_{xx}$ for 1% uniaxial strain along the x or y axis where $\Delta\epsilon_{xx} = \epsilon_{xx}(\text{strained}) - \epsilon_{xx}(\text{equilibrium})$. When the strain is along the x axis, the change is directly proportional to the elasto-optic coefficient p_{11} , while strain along the y axis describes p_{12} ; the data for $\Delta\epsilon_{yz}$ is generated by 1% shear strain and is proportional to p_{44} . Our conclusion

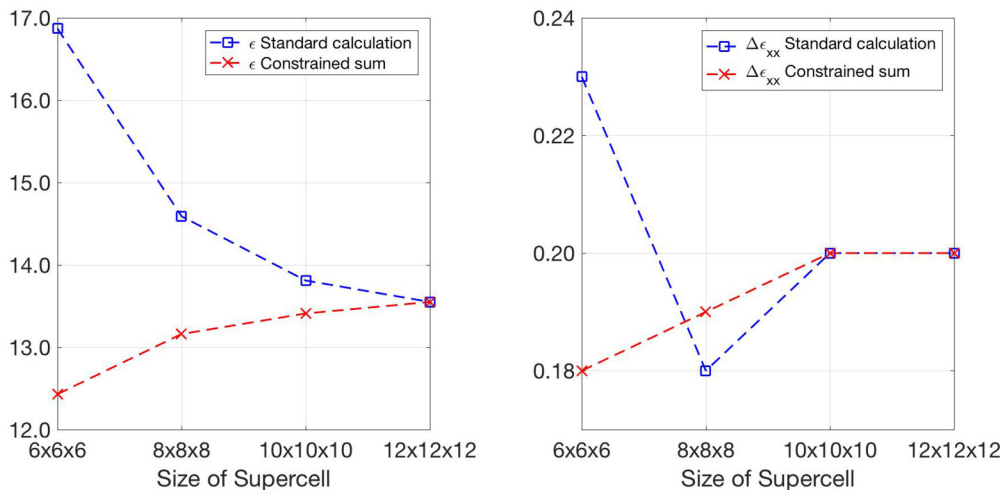


FIG. 5. Convergence of ϵ_{xx} and $\Delta\epsilon_{xx}$ with 1.0% uniaxial strain along the x axis in bulk Si using the Wannier function method.

TABLE VI. Three transition dipole matrix elements $|M|$ with the largest magnitude and their changes with different strain are listed in the second to fourth columns; the shell indices in the first column are those described in Fig. 6. The wave vector \mathbf{q} is along the x axis for the calculation of the matrix elements, so that $|M|$ is the magnitude of dipole transition vector projected on the x axis. In the last three columns, each row reports the cumulative contribution from the listed and preceding shells.

Dipole transition matrix elements	$ M $ (\AA)			Cumulative contribution to $\Delta\epsilon_{xx}$		Cumulative contribution to $\Delta\epsilon_{yz}$
	0% strain	$e_{xx} = 1\%$	$e_{yy} = 1\%$	$e_{xx} = 1\%$	$e_{yy} = 1\%$	$e_{yz} = 1\%$
"1" \rightarrow "1"	0.443	0.448	0.443	0.041	-9.4×10^{-3}	0.025
"1" \rightarrow "2"	0.174	0.176	0.175	0.083	2.8×10^{-3}	0.048
"1" \rightarrow "3"	0.169	0.171	0.168	0.152	-3.5×10^{-3}	0.039
All shells	—	—	—	0.199	-3.5×10^{-3}	0.094

is that the change in dielectric constant with strain is rather delocalized. First, the convergence with added shells is either slow (for strain along x) or nonmonotonic (for strain along y where the sign of the cumulative sum changes twice between the second and third shell). Second, although transitions on the same bond are the strongest, only including them does not provide quantitative accuracy. Third, while reasonable accuracy is obtained by summing up to the third shell of transitions, this involves a sum over nineteen independent transitions and, in our mind, is too complicated a physical picture to give insight for materials design in terms of photoelasticity. Hence, while the dielectric and elasto-optic response are spatially localized in Si, the length scale of the locality is too large and involves too many transitions for us to extract simple rules of thumb or provide simple guidance for designing elasto-optic response.

We now build upon this analysis protocol to analyze other materials with a primary focus on the degree of locality of the elasto-optic effect.

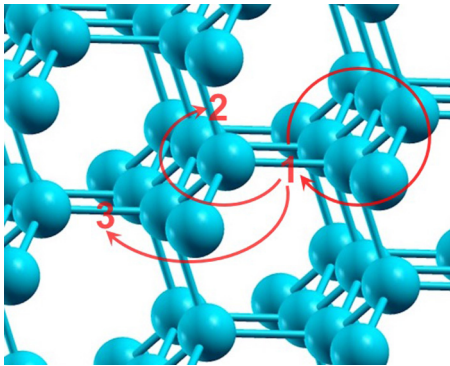


FIG. 6. The three shells of dipole transitions with the largest matrix elements in Wannier basis visualized in real space. Arrows are drawn from a bonding Wannier function (the initial state) to an antibonding Wannier function (the final state) of the dipole transition matrix elements. Given that the initial state is the bonding Wannier function on bond "1", the arrow "1" \rightarrow "1" illustrates the dipole transitions to the same bond (there is only one such type of transition per chemical bond), the arrow "1" \rightarrow "2" illustrates the dipole transitions to the nearest-neighbor bonds (there are six such transitions per chemical bond), and the arrow "1" \rightarrow "3" illustrates the dipole transitions to the second-nearest-neighbor bonds that are parallel to bond "1" (there are six such transitions per chemical bond).

VI. DIAMOND

Diamond, which shares the same crystal structure as silicon, serves as another example of a tetrahedral covalent insulator for our study of photoelasticity. The larger band gap and more localized atomic orbitals of diamond compared to Si give us hope that the elasto-optic response may be shorter ranged. We use the same methodology as we do for bulk Si.

The Wannier functions for bulk diamond are generated in a very similar manner as in Si, i.e., there are four bonding-antibonding Wannier function pairs per two-atom unit cell. Each pair consists of a bonding and an antibonding orbital centered around the same chemical bond between the neighboring carbon atoms. The computed band structure (see Fig. 7) shows that the four lowest conduction bands of diamond form an isolated group. Therefore the Wannier basis can describe both the valence bands and lowest four conduction bands exactly in diamond as shown in Fig. 7.

The dielectric constant for bulk diamond at equilibrium and its change with 1% strain along x axis are computed using Eq. (4). Table VII shows that the Wannier function method with a basis of four bonding and four antibonding agrees well with the RPA method with only eight bands included. Table VII also demonstrates the qualitative similarity of photoelasticity between bulk diamond and bulk Si. Namely, the dielectric constant changes in the same direction with 1% strain along x in both materials.

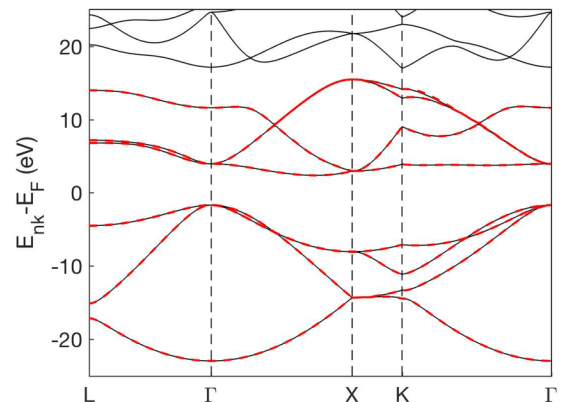


FIG. 7. Band structure of bulk diamond. Black solid lines are the DFT-LDA bands; red dashed lines are the Wannier interpolated bands. Both of the four valence and four lowest conduction bands form an isolated group of bands.

TABLE VII. Bulk diamond dielectric constant and its change with 1% uniaxial strain along the x axis obtained using DFPT, RPA with Bloch basis and with Wannier basis. The methods used are the same as Table IV. The results in the table are based on a $12 \times 12 \times 12$ k grid.

	DFPT	RPA (100 bands)	RPA (8 bands)	Wannier
$\epsilon(0.0\%)$	5.801	5.964	5.746	5.735
$\Delta\epsilon_{xx}(1.0\%)$	0.090	0.094	0.096	0.098
$\Delta\epsilon_{yy}(1.0\%)$	-0.020	-0.020	-0.023	-0.022

To further examine the spatial locality of diamond's dielectric response and to compare it with that of Si, the dipole transition matrix elements $|M|$ are computed using the Wannier basis. Figure 8 shows that, as expected, $|M|$ in diamond decays faster as a function of distance than Si. In addition, $6 \times 6 \times 6$ and $12 \times 12 \times 12$ supercells generate Wannier functions giving dipole transitions that are much closer in magnitude compared to Si (compare Figs. 4 and 8). Based on the physical picture developed above for bulk Si, this means that the Wannier functions in bulk diamond are more compact than in bulk Si, as expected due to diamond's wider band gap [34]. The superposition of the periodic images of the Wannier functions in the $6 \times 6 \times 6$ supercell still leads to dipole matrix elements that are quite accurate compared to those of the larger $12 \times 12 \times 12$ supercell. This indicates that the Wannier functions with their exponentially decaying tails are well contained in the $6 \times 6 \times 6$ supercell in diamond.

The compactness of the Wannier functions in diamond is also evident in the convergence calculation of the dielectric constant. The bulk diamond dielectric constant converges faster in both of the “standard” and “constrained sum” convergence calculation comparing to bulk Si (see Figs. 5 and 9). The increasing behavior of the dielectric constant (detailed above in the bulk Si results) is also observed using the “constrained sum” method (see the columns of Table VIII and Fig. 9 left panel). However, the change of the dielectric constant ϵ_{xx} along the x axis in diamond converges at a similar rate using the “constrained sum” method to Si. In fact, in both materials, the dipole transitions between the bonding and antibonding orbitals whose distance is within a $4 \times 4 \times 4$ supercell account for 80%–90% of the change in ϵ_{xx} due to uniaxial strain along the x axis.

Finally, just like Si, a “shell” analysis can be performed for bulk diamond. The diamond dipole transitions are first

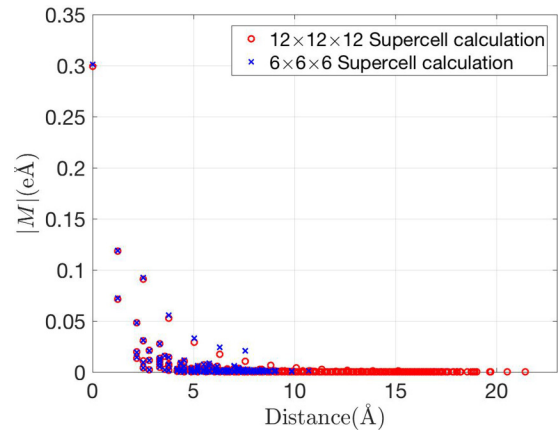


FIG. 8. Magnitude of the bulk diamond Wannier dipole matrix elements $|M|$ Eq. (5) versus distance between Wannier functions. Wave vector \mathbf{q} is aligned with x axis. The distance is between the center of $W_{b,0}$ (the bonding Wannier function in the home unit cell) and $W_{a,\mathbf{R}}$ (the antibonding Wannier function \mathbf{R} lattice vectors away). For reference, the bond length between nearest-neighbor C atoms is 1.55 \AA . The two sets of results are for Wannier functions generated in two different supercells.

grouped into shells that are defined in exactly the same way as bulk Si. Then, we identify the three different near-neighbor shells of dipole transitions that are largest in magnitude and also give the largest contribution to the dielectric constant (see Table IX). The cumulative contribution to the change of the dielectric constant using these three shells are also computed in Table IX. Though the Wannier functions are more compact in diamond than Si, our characterization of the spatial locality of the elasto-optic effect in diamond is to a great extent the same as silicon: one needs to sum up at least three shells' contribution to achieve reasonable accuracy for photoelasticity in bulk diamond.

VII. NaCl

The NaCl crystal serves as the first example of an ionic material for our study. It is a rocksalt structured, electronically closed-shell band insulator with the valence electrons filling bands of primarily Cl character. We use this chemical description to construct atom-centered Wannier functions for the valence bands, making one Wannier function have Cl s character and three Wannier functions have Cl p character. These four occupied Wannier functions can accommodate all the eight

TABLE VIII. Convergence of dielectric constant in bulk diamond using the Wannier RPA method. The table is in the same nomenclature as Table V.

		Size of supercell used to generate Wannier functions			
		$6 \times 6 \times 6$	$8 \times 8 \times 8$	$10 \times 10 \times 10$	$12 \times 12 \times 12$
Subset of Wannier functions used	$2 \times 2 \times 2$	3.38(0.05)	3.34(0.05)	3.34(0.05)	3.33(0.05)
	$4 \times 4 \times 4$	5.38(0.09)	5.25(0.08)	5.23(0.09)	5.23(0.09)
	$6 \times 6 \times 6$	6.04(0.10)	5.67(0.09)	5.64(0.09)	5.64(0.09)
	$8 \times 8 \times 8$		5.79(0.10)	5.72(0.10)	5.71(0.10)
	$10 \times 10 \times 10$			5.75(0.10)	5.73(0.10)
	$12 \times 12 \times 12$			–	5.74(0.10)

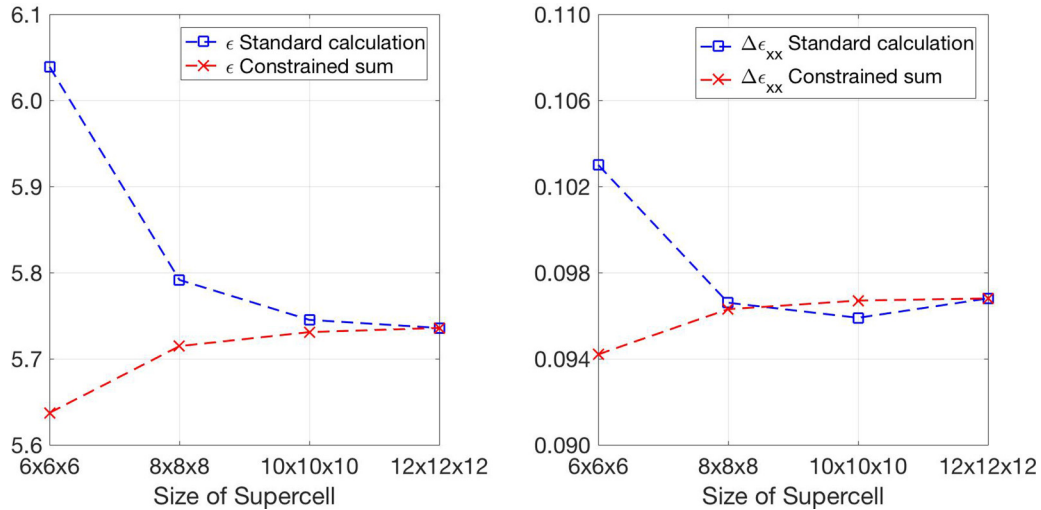


FIG. 9. Convergence of ϵ_{xx} and $\Delta\epsilon_{xx}$ with 1.0% uniaxial strain along the x axis in bulk diamond using the Wannier function method. The figure adopts the same notation as Fig. 5.

valence electrons (from both spin channels) in the two-atom fcc primitive unit cell. Though the conduction band edge is expected to have primarily Na $3s$ atomic orbital character, a quantitative description of the low-lying conduction bands is more complex. After examining the atomic projections of the low-lying conduction bands, we have decided to use one s -like and three p -like orbitals centered on the Na and five d -like orbitals centered on the Cl to construct the unoccupied Wannier basis. Figure 10 illustrates these occupied and unoccupied Wannier functions. The four occupied and nine unoccupied Wannier functions per unit cell can span the Hilbert space of the valence and lower part of the conduction bands. The band interpolation using the Wannier basis and its comparison to the DFT bands are shown in Fig. 11. The valence and five lowest conduction DFT bands are well reproduced by the Wannier basis but the four highest Wannier-derived conduction bands deviate from the corresponding DFT bands. Such discrepancy is normal and unavoidable: first, the Wannier disentanglement procedure hybridizes DFT bands to achieve the “smoothest” subspace across the Brillouin zone which tends to lead to narrower Wannier bands; second, higher conduction bands contain larger plane wave (free electron) character which becomes progressively harder to describe with any localized basis set leading to further discrepancies. We also point out that the choice of the Wannier representation of the conduction bands is not unique. Other sets of unoccupied

Wannier orbitals, e.g., the set of five d states on the Cl and one s state on Na or the set of five d states on Cl and two s states on the two interstitial sites half way between the Na and Cl

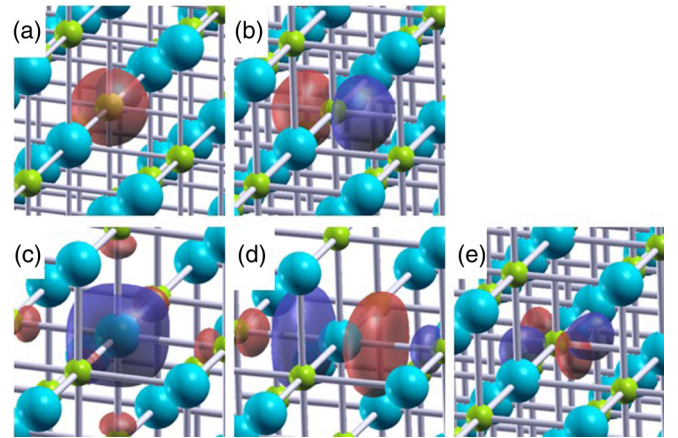


FIG. 10. Wannier functions in NaCl: occupied Wannier functions (a) Cl s orbital and (b) Cl p orbitals, unoccupied Wannier functions (c) Na s orbital, (d) a Na p orbitals, (e) a Cl d orbitals. Red and blue correspond to positive and negative value in these isosurface plots, respectively. These plots illustrate the atomic centered maximally localized Wannier functions. Color scheme of the atoms: Na: cyan, Cl: green.

TABLE IX. Three transition dipole matrix elements $|M|$ with largest magnitude and their changes with strain in bulk diamond are listed in the second to fourth column. The shells (in the first column) are indexed the same as bulk Si (see Table VI and Fig. 6). Last two columns of the table reports the cumulative contribution to $\Delta\epsilon_{xx}$ from the listed shells. The table follows the same notation as Table VI.

Dipole transition matrix elements	$ M $ (Å)			Cumulative contribution to $\Delta\epsilon_{xx}$	
	0% strain	1% x strain	1% y strain	1% x strain	1% y strain
“1” \rightarrow “1”	0.299	0.303	0.299	0.032	-6.7×10^{-3}
“1” \rightarrow “2”	0.119	0.118	0.119	0.052	-5.5×10^{-3}
“1” \rightarrow “3”	0.091	0.092	0.090	0.078	-11.9×10^{-3}
All shells	—	—	—	0.098	-22.2×10^{-3}

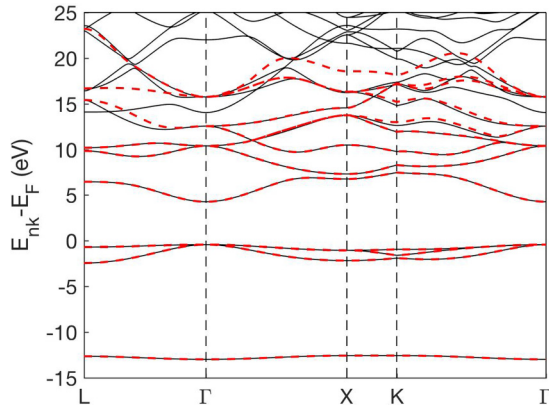


FIG. 11. Band structure of bulk rocksalt NaCl. Black solid lines are the DFT-LDA bands; red dashed lines are the Wannier interpolated bands. The valence Wannier bands are spanned by sp -like Wannier functions centered on Cl. The conduction Wannier bands are spanned by sp -like Wannier functions centered on Na and d -like Wannier functions centered on Cl.

along [111] direction, can interpolate at least the five lowest conduction bands very well. Our choice of the unoccupied Wannier functions gives the best numerical agreement for ϵ and $\Delta\epsilon$ between the RPA and Wannier methods, but the overall nature of the locality of photoelasticity in NaCl does not depend on which one of these Wannier representations is used.

Table X shows the comparison between the computed values of the dielectric constant and its change with 1% uniaxial strain using different methods. As noted above, the Wannier method agrees well with the RPA results using either a converged number of bands or 13 bands which is equal to the total number of orbitals in the Wannier basis. However, NaCl shows a qualitatively different elasto-optic response from the two tetrahedral covalent materials. The dielectric constant in NaCl decreases in the direction along which the tensile strain is applied opposite to the behavior of Si and diamond. The order of magnitude of $\Delta\epsilon_{xx}$ is also much smaller in NaCl than in Si and diamond. In fact, the change of ϵ is smaller in magnitude along the strain direction ($\Delta\epsilon_{xx}$) than in the perpendicular direction ($\Delta\epsilon_{yy}$).

Figure 12 shows that the magnitude of NaCl dipole transition matrix element $|M|$ is a very short-ranged function of the distance between Wannier function centers. In fact, $|M|$ drops to below 12% of its maximum magnitude when the occupied and unoccupied Wannier functions are further apart than the nearest neighbor Na-Cl distance. Furthermore, Wannier functions generated in the $6 \times 6 \times 6$ and the $12 \times$

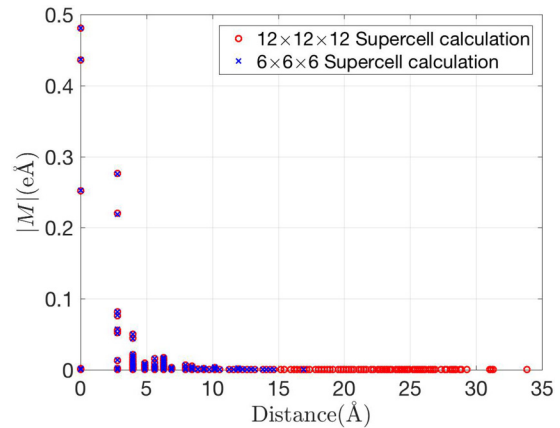


FIG. 12. Magnitude of the bulk NaCl Wannier dipole matrix elements $|M|$ versus distance between Wannier functions. The notations are the same as Fig. 4. For reference, the distance between neighboring Na and Cl atoms is 2.82 Å.

12×12 supercells virtually give the identical dipole matrix elements. Using the previous physical argument concerning Si and diamond, we conclude that the NaCl Wannier functions are quite compact, making the dipole transitions short-ranged between them.

The “standard” and “constrained sum” convergence results for the dielectric response are reported in Table XI and Fig. 13 for both ϵ and $\Delta\epsilon_{xx}$. As expected, the compactness of the NaCl Wannier functions leads to a rapid convergence of ϵ using both the “standard” and “constrained sum” methods. The change of the dielectric constant $\Delta\epsilon_{xx}$ also converges rapidly using the “constrained sum” method (see Fig. 13), making the locality of the change of the dielectric constant evident. However, the right panel of Fig. 13 shows that “standard” calculation of $\Delta\epsilon_{xx}$ converges more slowly versus supercell size, suggesting that subtle changes of the Wannier functions with strain can only be captured using the large $12 \times 12 \times 12$ supercell. Therefore the previous conclusion for locality in the elasto-optic response carries over from Si and diamond to NaCl: a large enough supercell is needed to generate the Wannier functions, and we should use the “constrained sum” method to sum up the local contributions in ϵ and $\Delta\epsilon$ in a predictable manner.

Last but not the least, the “shell” analysis can be performed for NaCl. Since the Wannier functions are atom-centered in NaCl, the shells can be labeled by the atomic sites between which the dipole transitions take place. The three shells contributing the largest magnitudes to both ϵ and $\Delta\epsilon$ are illustrated with arrows in Fig. 14. The cumulative contribu-

TABLE X. Bulk rocksalt NaCl dielectric constant and its change with 1% uniaxial strain along x axis obtained using DFPT, RPA with Bloch states in a plane wave basis and with the Wannier basis. These methods are the same as those in Tables IV and VII. The results in the table are based on a $12 \times 12 \times 12$ k grid.

	DFPT	RPA (100 bands)	RPA (13 bands)	Wannier
$\epsilon(0.0\%)$	2.51	2.81	2.77	2.79
$\Delta\epsilon_{xx}(1.0\%)$	-3.7×10^{-3}	-5.4×10^{-3}	-6.3×10^{-3}	-5.6×10^{-3}
$\Delta\epsilon_{yy}(1.0\%)$	-9.6×10^{-3}	-10.5×10^{-3}	-11.1×10^{-3}	-10.7×10^{-3}

TABLE XI. Convergence with supercell size of the dielectric constant and its strain dependence in bulk NaCl using the Wannier function method. This table uses the same nomenclature as Tables V and VIII.

		Size of supercell used to generate Wannier functions			
		6 × 6 × 6	8 × 8 × 8	10 × 10 × 10	12 × 12 × 12
Subset of Wannier functions used	2 × 2 × 2	2.16(−1.8 × 10 ^{−3})	2.17(−2.7 × 10 ^{−3})	2.17(−2.4 × 10 ^{−3})	2.16(−3.4 × 10 ^{−3})
	4 × 4 × 4	2.75(−3.5 × 10 ^{−3})	2.75(−6.9 × 10 ^{−3})	2.76(−5.7 × 10 ^{−3})	2.75(−5.1 × 10 ^{−3})
	6 × 6 × 6	2.79(−4.1 × 10 ^{−3})	2.79(−7.3 × 10 ^{−3})	2.79(−6.1 × 10 ^{−3})	2.79(−5.5 × 10 ^{−3})
	8 × 8 × 8		2.79(−7.4 × 10 ^{−3})	2.79(−6.1 × 10 ^{−3})	2.79(−5.6 × 10 ^{−3})
	10 × 10 × 10			2.79(−6.1 × 10 ^{−3})	2.79(−5.6 × 10 ^{−3})
	12 × 12 × 12				2.79(−5.6 × 10 ^{−3})

tions to the change of the dielectric constant using these three shells are found in Table XII. Since each atomic site hosts more than one kind of Wannier functions in NaCl, there exists multiple inequivalent dipole transitions within each shell with differing dipole elements, and therefore the values for the dipole matrix elements are omitted in Table XII. We can see from the table that even in an ionic insulator like NaCl with very compact Wannier functions, in order to converge $\Delta\epsilon$ to a satisfactory accuracy, one must still sum the first three shells' contribution which includes dipole transitions between second-nearest neighbor atoms. (However, if we seek only an

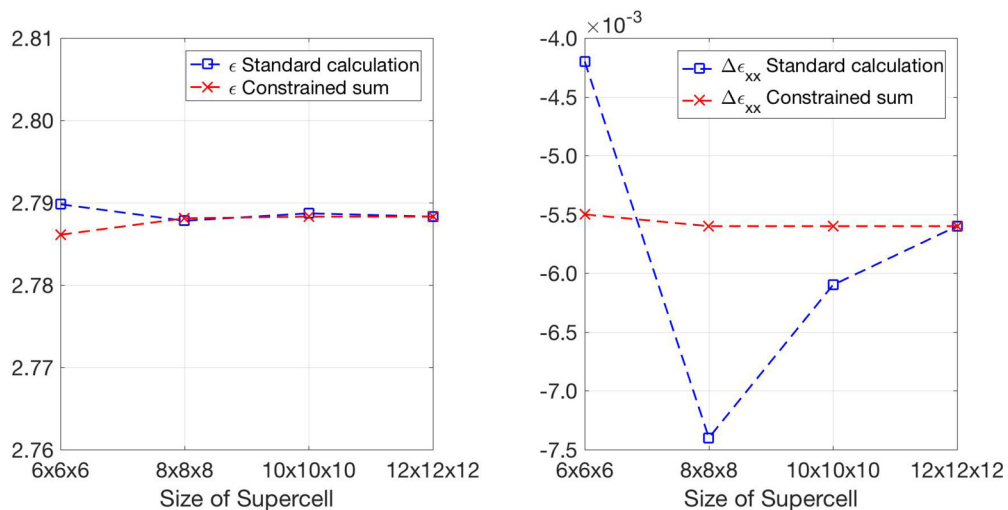
order of magnitude estimate with correct sign, two shells are sufficient.)

VIII. MgO

MgO shares the same crystal structure as NaCl and has very similar chemical properties. It is a rocksalt structured, closed-shell band insulator with its valence electrons filling bands with mostly O character. In fact, after projecting the bands onto atomic-like orbitals, we find that a Wannier basis similar to the one for NaCl is also an appropriate choice for MgO: for occupied Wannier functions, we use one orbital with O *s* character and three orbitals with O *p* character to describe the valence bands; for unoccupied Wannier functions, we use one *s*-like and three *p*-like orbitals centered on Mg and five *d*-like orbitals centered on O to describe the low energy conduction bands. The DFT band structure and its Wannier interpolation are shown in Fig. 15. One can see that the valence bands and lowest three conduction bands are accurately reproduced by the Wannier basis. The discrepancies between higher conduction bands and Wannier bands are attributed to the fact that there is more plane wave character in higher conduction bands, making for difficulties for any localized basis set.

TABLE XII. The cumulative contribution to $\Delta\epsilon_{xx}$ of three shells of dipole transitions are shown in the table for NaCl. The shell indices in the first column correspond to those described in Fig. 14. The table follows the same notation as Table VI's last two columns.

Dipole transition matrix elements	Cumulative contribution to $\Delta\epsilon_{xx}$	
	1% <i>x</i> strain	1% <i>y</i> strain
“1” → “1”	−1.9 × 10 ^{−3}	−5.4 × 10 ^{−3}
“1” → “2”	−1.9 × 10 ^{−3}	−7.7 × 10 ^{−3}
“1” → “3”	−4.4 × 10 ^{−3}	−10.0 × 10 ^{−3}
All shells	−5.6 × 10 ^{−3}	−10.7 × 10 ^{−3}

FIG. 13. Convergence of ϵ_{xx} and $\Delta\epsilon_{xx}$ with 1.0% uniaxial strain along the *x* axis in bulk NaCl using the Wannier function method. The figure uses the same notations as Fig. 5.

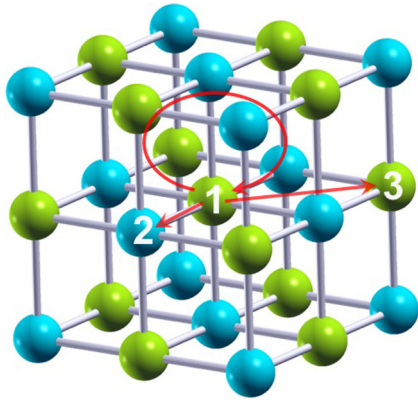


FIG. 14. The three shells of dipole transitions in bulk NaCl with the largest matrix elements in the Wannier basis visualized in real space. Color scheme of the atoms: Na: cyan and Cl: green. Similar to Fig. 6, the arrows are drawn from the centers of the occupied Wannier function (initial state on Cl) to the centers of the unoccupied Wannier functions (final state on either Cl or Na) of the dipole transition. Each individual atomic site corresponds to multiple occupied and unoccupied Wannier functions in NaCl (unlike in bulk Si and diamond where each chemical bond accommodates a unique pair of bonding and antibonding Wannier functions). With an initial occupied Wannier function on Cl atom “1”, the arrow “1” \rightarrow “1” illustrates the dipole transitions to the same atom (from the sp states to the d states of the same Cl atom), “1” \rightarrow “2” illustrates the dipole transitions to the nearest-neighbor Na atoms (from the sp states of Cl to the sp states of the neighboring Na atoms), and “1” \rightarrow “3” illustrates the dipole transitions to the second-nearest-neighbor Cl atoms (from the sp states of Cl to the d states of its second-nearest-neighbor Cl atoms).

Table XIII shows how the dielectric constant changes with uniaxial strain in MgO computed using various methods. As expected, the Wannier method agrees well with RPA method with either converged number of bands or 13 bands which

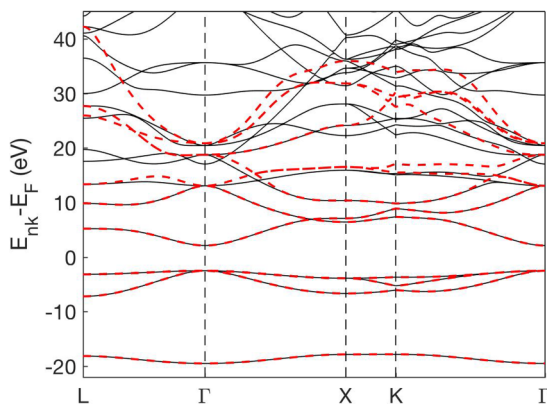


FIG. 15. Band structure of bulk rocksalt MgO. Black solid lines are the DFT-LDA bands; red dashed lines are the Wannier interpolated bands. The valence Wannier bands are spanned by sp -like Wannier functions centered on O. The conduction Wannier bands are spanned by sp -like Wannier functions centered on Mg and d -like Wannier functions centered on O.

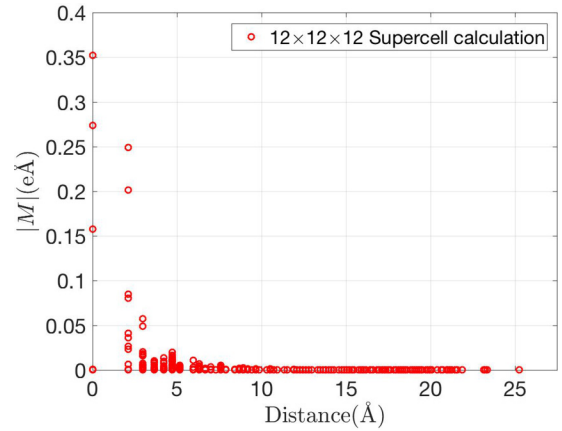


FIG. 16. Magnitude of the bulk MgO Wannier dipole matrix elements $|M|$ vs distance between Wannier functions. The notations are the same as Fig. 4. For reference, the distance between neighboring Mg and O atoms is 2.11 Å.

is equal to the total number of orbitals in the Wannier basis, just like discussed above in Si, diamond, and NaCl. However, MgO has the opposite elasto-optic response to NaCl in both p_{11} and p_{12} components: the dielectric constant of MgO increases both along and perpendicular to the tensile strain direction. In addition, the $\Delta\epsilon$ has much larger magnitude along the strain ($\Delta\epsilon_{xx}$ in Table XIII) than perpendicular to the strain ($\Delta\epsilon_{yy}$ in Table XIII). This difference between NaCl and MgO must originate from the chemistry of the different constituting atoms of the two materials and is a subject for future work.

The “standard” convergence calculation using different k grid has been performed for Si, diamond, and NaCl, and similar physical conclusions about the locality have been drawn from the relationship between the “standard” and “constrained sum” methods for all three materials. Hence, the calculations for MgO are done only based a dense $12 \times 12 \times 12$ k grid. Figure 16 shows that the dipole transition matrix element $|M|$ is very short-ranged, suggesting that the Wannier basis is also very localized in MgO.

Table XIV and Fig. 17 report the spatial locality of ϵ and $\Delta\epsilon_{xx}$ with 1% strain along the x axis using the “constrained sum” method. As observed above, a spatial convergence of ϵ is obtained by progressively summing the contributions of dipole transitions with increasing distance. However, it is critical to emphasize that despite the sensible locality of dielectric and elasto-optic response, one must still include the dipole transitions in the $4 \times 4 \times 4$ supercell to achieve good convergence in both ϵ and $\Delta\epsilon_{xx}$.

The “shell” analysis results are shown in Table XV. Since MgO and NaCl both have the rocksalt crystal structure, we can label their “shells” in exactly the same way. Although in MgO, $\Delta\epsilon$ converges versus added shells at a similar rate to NaCl, the MgO dielectric responds to the strain in the opposite direction to NaCl as noted above in Table XIII. In addition, the $\Delta\epsilon$ perpendicular to strain converges nonmonotonically with shells, which makes the photoelasticity long-ranged in MgO.

TABLE XIII. Bulk rocksalt MgO dielectric constant and its change with 1% uniaxial strain along the x axis obtained using DFPT, RPA with Bloch states in a plane wave basis and with the Wannier basis. These methods are the same as those in Tables IV and VII. The results in the table are based on a $12 \times 12 \times 12$ k grid.

	DFPT	RPA (100 bands)	RPA (13 bands)	Wannier
$\epsilon(0.0\%)$	3.13	3.25	3.18	3.21
$\Delta\epsilon_{xx}(1.0\%)$	3.0×10^{-2}	3.0×10^{-2}	2.9×10^{-2}	3.1×10^{-2}
$\Delta\epsilon_{yy}(1.0\%)$	0.4×10^{-2}	0.4×10^{-2}	0.4×10^{-2}	0.5×10^{-2}

IX. SUMMARY AND OUTLOOK

In this paper, we have developed a method to calculate the dielectric and elasto-optic response of solids within the RPA using a maximally localized Wannier function basis. Compared with state-of-the-art DFPT method, RPA in the Wannier basis achieves a satisfactory numerical accuracy while presenting a simple analytical expression that highlights the role of dipole transitions between the occupied and unoccupied Wannier functions. By organizing the dipole transitions into shells according to the distances between the occupied and unoccupied Wannier functions, both of the dielectric and photoelastic responses systematically converge within the “constrained sum” method and their spatial behavior is sensible. We have discovered that elasto-optic responses are rather delocalized in the Maximally Localized Wannier basis: in Si, diamond, NaCl, and MgO, we must sum the cumulative contributions of at least three spatially localized shells to converge $\Delta\epsilon$ to a reasonable precision. Moreover, the convergence with increasing shells is not monotonic in some cases (e.g., p_{12} in Si and MgO). Silicon’s long-tailed Wannier functions, which need to be generated in a relatively large supercell, lead to the long-ranged behavior of its photoelasticity. However, in spite of the Wannier functions being quite compact in diamond, NaCl, and MgO, the locality of their elasto-optic response is at a similar scale to bulk Si: one must sum up to 3 shells’ contribution to converge the change of dielectric constant with reasonable precision. The length scale of locality in the maximally localized Wannier basis is too large and contains too many dipole transitions for us to extract simple material design rules for photoelasticity. This is in contrast to the locality of the electronic polarizability in the MLWF basis [46] where a nearest-neighbor only model

is already quantitatively accurate. However, not all is lost: while not localized as one would like on individual atoms and chemical bonds, the real-space Wannier description is far more localized than the k -space description for describing the dielectric and photoelastic response, and a reasonably-sized nanocluster of the material (i.e., up to the third shell of nearest-neighbors) is sufficient to describe the photoelastic response. In addition, we have discovered some unexpected photoelastic behaviors, e.g., Tables XII and XV show that NaCl and MgO have opposite photoelastic responses, or that there is a nonmonotonic convergence with increasing number of space shells for the p_{12} component in Si, diamond, and MgO. Despite significant effort, at present we are unable to explain these unexpected behaviors and hope that future work will elucidate the situation.

There is an existing literature that uses highly localized bond orbital tight-binding models to compute dielectric response in solids [19,47] that can be extended to photoelastic response. For example, the empirical model for the strain dependencies of dielectric response by Damas *et al.* [18] assumes a nearest-neighbor tight-binding model in tetrahedral semiconductors based on bond orbital theory for Si. They build a 2×2 Hamiltonian with fitting parameters with two sp^3 hybrid orbitals on neighboring atoms as the basis to describe the bond polarizability, and the free parameters are fit to photoelasticity experiments. Since this model only includes the first shell of contribution for dielectric response, which according to our work is microscopically inadequate, the effects of higher order shells must be strongly renormalizing the values of the empirical parameters. Such a compact description can help us understand *a posteriori* the photoelasticity of known materials where experimental values are

TABLE XIV. Convergence with supercell size of the dielectric constant and its strain dependence in bulk MgO using the Wannier function method. The “standard” convergence calculation is not performed for MgO. The results in the table are all based on the $12 \times 12 \times 12$ k grid calculation. This table uses the same nomenclature as Table V.

	Size of supercell used to generate Wannier functions $12 \times 12 \times 12$
	$2 \times 2 \times 2$
	$4 \times 4 \times 4$
Subset of	$6 \times 6 \times 6$
Wannier functions used	$8 \times 8 \times 8$
	$10 \times 10 \times 10$
	$12 \times 12 \times 12$

$\mathbf{q} \rightarrow 0$, which is not guaranteed by numerical diagonalization procedures used in standard electronic structure calculations (e.g., when using QUANTUM ESPRESSO). Generally, the computed Bloch states on two k point grids are related to each other through a unitary transformation:

$$\langle \psi_{m,\mathbf{k}} | \psi_{n,\mathbf{k}+\mathbf{q}} \rangle = Q_{mn}^{(\mathbf{k})},$$

where $Q^{(\mathbf{k})} \times Q^{(\mathbf{k})\dagger} = Q^{(\mathbf{k})\dagger} \times Q^{(\mathbf{k})} = I$ when $\mathbf{q} \rightarrow 0$. The “natural” gauge can be restored easily by performing a unitary transformation (only needed for the shifted valence

bands):

$$\tilde{\psi}_{v,\mathbf{k}+\mathbf{q}} = \sum_{v'} \psi_{v',\mathbf{k}+\mathbf{q}} \times Q_{v'v}^{(\mathbf{k})\dagger},$$

where v, v' range over valence band indices. We use such unitary rotated valence bands $\tilde{\psi}$ when computing off-diagonal dielectric tensor components such as ϵ_{yz} (for diagonal components, there is only a single shifted k grid so the issue of the natural gauge does not arise).

-
- [1] H. G. Limberger, P. Fojallaz, R. P. Salathé, and F. Cochet, *Appl. Phys. Lett.* **68**, 3069 (1996).
- [2] H. J. Peng, S. P. Wong, Y. W. Lai, X. H. Liu, H. P. Ho, and S. Zhao, *Rev. Sci. Instrum.* **74**, 4745 (2003).
- [3] P. T. Rakich, P. Davids, and Z. Wang, *Opt. Express* **18**, 14439 (2010).
- [4] M. Li, W. H. P. Pernice, C. Xiong, T. Baehr-Jones, M. Hochberg, and H. X. Tang, *Nature (London)* **456**, 480 (2008).
- [5] I. El-Kady, R. H. Olsson, and J. G. Fleming, *Appl. Phys. Lett.* **92**, 233504 (2008).
- [6] M. Eichenfield, R. Camacho, J. Chan, K. J. Vahala, and O. Painter, *Nature (London)* **459**, 550 (2009).
- [7] M. Eichenfield, C. P. Michael, R. Perahia, and O. Painter, *Nat. Photon.* **1**, 416 (2007).
- [8] J. Chan, M. Eichenfield, R. Camacho, and O. Painter, *Opt. Express* **17**, 3802 (2009).
- [9] A. Erba and R. Dovesi, *Phys. Rev. B* **88**, 045121 (2013).
- [10] Z. H. Levine, H. Zhong, S. Wei, D. C. Allan, and J. W. Wilkins, *Phys. Rev. B* **45**, 4131 (1992).
- [11] J. E. Reynolds, Z. H. Levine, and J. W. Wilkins, *Phys. Rev. B* **51**, 10477 (1995).
- [12] Z. H. Levine, J. H. Burnett, and E. L. Shirley, *Phys. Rev. B* **68**, 155120 (2003).
- [13] D. Donadio, M. Bernasconi, and F. Tassone, *Phys. Rev. B* **68**, 134202 (2003).
- [14] P. Hohenberg and W. Kohn, *Phys. Rev.* **136**, B864 (1964).
- [15] L. J. Sham and W. Kohn, *Phys. Rev.* **140**, A1133 (1965).
- [16] S. Baroni, S. de Gironcoli, A. Dal Corso, and P. Giannozzi, *Rev. Mod. Phys.* **73**, 515 (2001).
- [17] D. Donadio, M. Bernasconi, and F. Tassone, *Phys. Rev. B* **70**, 214205 (2004).
- [18] P. Damas, D. Marris-Morini, E. Cassan, and L. Vivien, *Phys. Rev. B* **93**, 165208 (2016).
- [19] W. A. Harrison, *Phys. Rev. B* **8**, 4487 (1973).
- [20] N. Marzari, A. A. Mostofi, J. R. Yates, I. Souza, and D. Vanderbilt, *Rev. Mod. Phys.* **84**, 1419 (2012).
- [21] W. A. Harrison, *Electronic Structure and the Properties of Solids: the Physics of the Chemical Bond* (Dover, 1989).
- [22] T. S. Narasimhamurthy, *Photoelastic and Electro-Optic Properties of Crystals* (Springer, US, 1981).
- [23] P. Giannozzi, S. Baroni, N. Bonini, M. Calandra, R. Car, C. Cavazzoni, Davide Ceresoli, G. L. Chiarotti, M. Cococcioni, I. Dabo, A. D. Corso, S. d. Gironcoli, S. Fabris, G. Fratesi, R. Gebauer, U. Gerstmann, C. Gougoussis, Anton Kokalj, M. Lazzeri, L. Martin-Samos, N. Marzari, F. Mauri, R. Mazzarello, Stefano Paolini, A. Pasquarello, L. Paulatto, C. Sbraccia, S. Scandolo, G. Sclauzero, A. P. Seitsonen, A. Smogunov, P. Umari, and R. M. Wentzcovitch, *J. Phys.: Condens. Matter* **21**, 395502 (2009).
- [24] D. M. Ceperley and B. J. Alder, *Phys. Rev. Lett.* **45**, 566 (1980).
- [25] J. P. Perdew and A. Zunger, *Phys. Rev. B* **23**, 5048 (1981).
- [26] J. P. Perdew and Y. Wang, *Phys. Rev. B* **45**, 13244 (1992).
- [27] U. von Barth and C. D. Gelatt, *Phys. Rev. B* **21**, 2222 (1980).
- [28] N. Troullier and J. L. Martins, *Phys. Rev. B* **43**, 1993 (1991).
- [29] A. D. Mighell and V. L. Karen, *J. Res. Natl. Inst. Stand. Technol.* **101**, 273 (1996).
- [30] S. Adler, *Phys. Rev.* **126**, 413 (1962).
- [31] N. Wiser, *Phys. Rev.* **129**, 62 (1963).
- [32] N. Marzari and D. Vanderbilt, *Phys. Rev. B* **56**, 12847 (1997).
- [33] I. Souza, N. Marzari, and D. Vanderbilt, *Phys. Rev. B* **65**, 035109 (2001).
- [34] S. Ismail-Beigi and T. A. Arias, *Phys. Rev. Lett.* **82**, 2127 (1999).
- [35] A. A. Mostofi, J. R. Yates, Y.-S. Lee, I. Souza, D. Vanderbilt, and N. Marzari, *Comput. Phys. Commun.* **178**, 685 (2008).
- [36] A. A. Mostofi, J. R. Yates, G. Pizzi, Y.-S. Lee, I. Souza, D. Vanderbilt, and N. Marzari, *Comput. Phys. Commun.* **185**, 2309 (2014).
- [37] D. K. Biegelsen, *Phys. Rev. Lett.* **32**, 1196 (1974).
- [38] H. R. Philipp and E. A. Taft, *Phys. Rev.* **127**, 159 (1962).
- [39] R. S. Leigh and B. Szigeti, *J. Phys. C: Solid State Phys.* **3**, 782 (1970).
- [40] K. G. Aggarwal and B. Szigeti, *J. Phys. C: Solid State Phys.* **3**, 1097 (1970).
- [41] L. Benckert and G. Bäckström, *Phys. Rev. B* **8**, 5888 (1973).
- [42] K. Vedam and E. D. D. Schmidt, *Phys. Rev.* **146**, 548 (1966).
- [43] A. A. Giardini and E. Poindexter, *JOSA* **48**, 556 (1958).
- [44] K. V. K. Rao and V. G. K. Murty, *Acta Crystallogr.* **17**, 788 (1964).
- [45] F. Detraux and X. Gonze, *Phys. Rev. B* **63**, 115118 (2001).
- [46] X. Ge and D. Lu, *Phys. Rev. B* **92**, 241107(R) (2015).
- [47] M. E. Lines, *Phys. Rev. B* **41**, 3372 (1990).